Characteristic curves of the Mie fluid

Simon Stephan[a)] and Maximilian Urschel

Laboratory of Engineering Thermodynamics (LTD), RPTU Kaiserslautern,

67663 Kaiserslautern, Germany

Brown's characteristic curves of the Mie n, m fluid were investigated using molecular dynamics (MD) simulation and a molecular-based equation of state. Both, the 0th-order (Zeno) and three 1st-order characteristic curves (Amagat, Boyle, and Charles) were studied. The study was carried out using a hybrid approach combining MD simulation and molecular theory. Thereby, exact values for the zero-density limit of the characteristic curves were obtained using the second virial coefficient route. The focus was on the variation of the repulsive exponent of the Mie potential with $n = 8, 10, 11, 12, 13, 14, 16, 20, 36, 48$ (dispersive exponent constant at $m = 6$). Also, the influence of the dispersive exponent on the characteristic curves was studied with $m = 4, 5, 6, 7, 8$ (repulsive exponent constant at $n = 12$). In total, 14 Mie fluids were studied. Based on the results, the influence of the shape of the intermolecular potential on the macroscopic properties, i.e. the characteristic curves, is elucidated. Interestingly, the Amagat curve is found to exhibit a peculiar dependency on the repulsive exponent. However, the postulates of Brown regarding the form and regularities of the characteristic curves are confirmed for all studied Mie fluids. Furthermore, the applicability of the classical corresponding states principle is assessed using the characteristic curve data. Important differences are obtained for the two exponents: The corresponding states principle captures reasonably well the variation of the dispersive exponent, but fails for describing the influence of the repulsive exponent. The results from this work are compared with predictions from a molecular-based equation of state, which is found to perform well in almost all studied cases.

Keywords: Mie potential, molecular dynamics simulation, Brown's characteristic curves

---

[a)]Electronic mail: Simon.Stephan@rptu.de

I. INTRODUCTION

The Mie fluid is an important model fluid that is also frequently used for modeling real substances using both classical force fields[1–5] and molecular-based equations of state[6,7]. The Mie potential u_{Mie} is defined as[8,9]

$$u_{\mathrm{Mie}}(r) = \frac{n}{n-m}\left(\frac{n}{m}\right)^{\frac{m}{n-m}} \varepsilon \left[\left(\frac{\sigma}{r}\right)^n - \left(\frac{\sigma}{r}\right)^m\right], \tag{1}$$

with σ and ε being the size and energy parameter, respectively, and n and m being the repulsive and dispersive exponents, respectively. The distance between two particles is denoted by r. The repulsive exponent n primarily describes the softness of the potential, i.e. the repulsive interactions become harder with increasing n. The dispersive exponent m primarily describes the range of the potential as well as the strength of the attractive force at intermediate range since the dispersion energy is prescribed by ε. The influence of the two parameters n and m on the potential shape is depicted in Fig. 1.
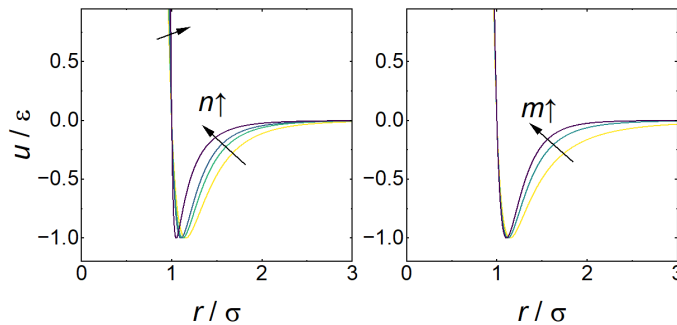

FIG. 1: Examples of the Mie n, m potential. Left: Variation of repulsive exponent (n = $8, 12, 16, 48$ and $m = 6$); Right: Variation of dispersive exponent ($n = 12$ and $m = 4, 6, 8$).

The Mie potential is the generalized version of the Lennard-Jones (LJ) potential, which has – since the early days of computational molecular thermodynamics[10,11] – been extensively studied in the literature[12,13]. Interestingly, the Mie potential predates the Lennard-Jones potential historically[6,8,9]. In the Mie potential, the classical $n = 12$, $m = 6$ exponents of the LJ potential are variable parameters. In the LJ potential, the choice for the dispersive exponent $m = 6$ is physically motivated[14], whereas the repulsive exponent $n = 12$ was originally primarily chosen for computational convenience.

The idea of the Mie potential is to algebraically describe repulsion and dispersion by two separate terms and their exponents, cf. Eq. (1). Nevertheless, both terms influence the

potential form in the entire range of r. This can also be seen in Fig. 1: The variation of the repulsive exponent n also influences the form of the potential in the attractive part and the dispersive exponent m also influences the repulsive part of the potential. The latter is, however, less prominent. Overall, Fig. 1 shows that the two exponents influence the form of the potential in a complex way. Increasing n yields not only an increasing steepness of the repulsion, but also a decrease of the effective particle size and a shift of the attractive part. Thereby, the potential becomes more narrow with increasing n. Both increasing n and m result effectively in a decreasing range of attraction, i.e. the potential converges to zero at shorter distances (cf. Fig. 1).

Due to the practical importance of the Mie potential, the influence of the potential parameters m, n on macroscopic material properties has been frequently studied in the literature. The vapor-liquid equilibrium (VLE) and interface has been studied several times[15–19]. Also data on the solid-liquid equilibrium of the Mie fluid is available[20]. *Sadus*[21] as well as *Heyes et al.*[22] have studied the second virial coefficient of special Mie n, m fluids. Also homogeneous bulk phase properties have been studied at times, e.g. Refs.[23–26]. *Apfelbaum and Vorob'ev* have studied the behavior of the Zeno curve in the density-temperature plane of Mie $n, 6$ fluids[27]. In general, the exponents of the potential are known to have an important influence on thermodynamic derivative properties such as the compressibility[6] and heat capacity[26].

No information is presently available on the influence of the two Mie potential exponents on Brown's characteristic curves (except for the Zeno curve[27]). Brown proposed the characteristic curves for the evaluation of thermodynamic models for fluids with solely repulsive and dispersive interactions[28]. Brown's characteristic curves have since then become an important tool for testing the extrapolation behavior of new equation of state models – also exhibiting more complex molecular interactions[29–32]. The testing of Brown's characteristic curves has also been included in the IUPAC guidelines for publishing equations of state[33]. At times, also other names are used for the four characteristic curves, i.e. the Zeno curve is also called *ideal curve*, the Amagat curve *Joule inversion curve*, and the Charles curve is often called *Joule-Thomson inversion curve*. In this work, the terminology introduced by Brown[28] is used.

According to Brown, one 0th-order curve (called Zeno curve) and three 1st-order characteristic curves (called Amagat, Boyle, and Charles curve) exist. The characteristic curves are defined as the loci of state points at which a certain thermodynamic property of the

fluid equals that of an ideal gas[28,30,34]. As a result of Gibbs' phase rule, the compressibility factor Z and its derivatives with respect to temperature, density, and pressure match the values of the ideal gas for special temperature and density combinations only, which constitutes the characteristic curves. Multiple thermodynamically equivalent conditions apply to a characteristic curve[35], e.g. $Z = 1$ for the Zeno curve, $(\partial Z/\partial V)_T = 0$ for the Boyle curve, $(\partial H/\partial p)_T = 0$ for the Charles curve, and $(\partial U/\partial V)_T = 0$ for the Amagat curve. Details on the thermodynamic derivation and relations are given in the Supplementary Material and can be found elsewhere[28,30,34,36,37].

Fig. 2 schematically shows the four characteristic curves in the $p - T$ projection as well as their relation to the second virial coefficient. Brown's characteristic curves cover a range of multiple orders of magnitude in temperature and pressure. Based on rational thermodynamic arguments, Brown derived a number of necessary conditions for the characteristic curves of a simple molecular fluid (as depicted in Fig. 2)[28,37]: In a double-logarithmic pressure–temperature diagram, the Zeno, Amagat, Boyle, and Charles curve are required to have a single maximum, exhibit negative curvature throughout, and end with infinite slope in the zero-density limit. Moreover, the Zeno curve contacts the three 1st-order curves in a single state point only[28,37,38]. The three 1st-order curves may not contact each other. Moreover, the Charles curve and the Boyle curve intersect the VLE, cf. Fig. 2. Hence, Brown postulated the behavior and shape of the characteristic curves for a generalized simple repulsive-dispersive fluid. Yet, details of the form of the potential will in general influence the characteristic curves. The Mie fluid is an excellent candidate for investigating the nature of Brown's characteristic curves and their relation to the detailed form of the intermolecular potential.

Brown's characteristic curves themselves are also relevant for technical applications. The Charles curve is also known as the Joule-Thomson inversion curve and crucial for energy conversion technology[39–41] as it is defined as the locus of state points, where the temperature change upon isenthalpic throttling changes from heating to cooling. Also, the range of the characteristic curves is relevant for tribological[42,43] and geological applications[37]. For low-boiling fluids such as neon, helium, and hydrogen, the range of all four characteristic curves is also applicable for technical applications at moderate thermodynamic conditions.

There is practically no experimental data available for Brown's characteristic curves (only, for the Joule-Thomson inversion curve, some data is available[44]). Computational studies of
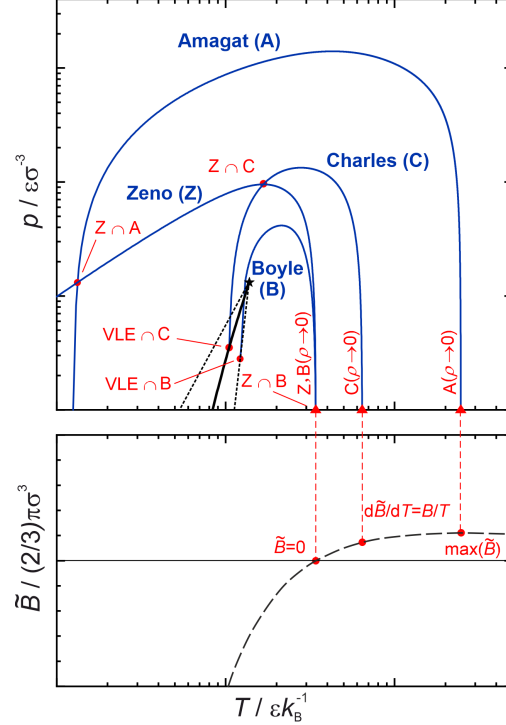
FIG. 2: Scheme of Brown's characteristic curves (top) and their relation to the second virial coefficient (bottom). For the top plot: Blue lines indicate the characteristic curves; black color indicates the vapor-liquid equilibrium (star indicates the critical point, dotted lines the spinodal, and solid line the binodal). Special points on the characteristic curves are indicated as red circles.

the characteristic curves have been carried out at times: *Stephan and Deiters* studied the characteristic curves of the classical Lennard-Jones potential[30]. *Deiters* and co-workers have also assessed the behavior of different equation of state models regarding the characteristic curves[33,34]. *Apfelbaum* and co-workers have studied special features of Brown's characteristic (and other similar curves) of fluids[45–48]. Several studies are available that report molecular simulation data for the Joule-Thomson inversion (a.k.a. Charles) curve[39,40,49–56]. First principle data for the entire set of characteristic curves is still very scarce. *Deiters and Neumann* used for the first time molecular simulations (Monte Carlo) to predict the entire set of Brown's characteristic curves for simple model fluids[37]. In a recent work of our group, we have proposed a rigorous approach for determining Brown's characteristic curves combining classical molecular dynamics simulations for determining the characteristic curves in the entire temperature range with rigorous statistical mechanics to determine the exact

5

zero-density limits of the characteristic curves[35]. Thereby, the thermodynamic behavior of a given fluid can be characterized and assessed in a large temperature and pressure range.

The classical corresponding states principle can be used to model fluid properties based on the observation that molecular fluids show a similar behavior when compared at the same reduced temperature and reduced pressure with respect to the critical values[57,58]. Yet, the corresponding states principle is not a general rigorous law, but is well known to yield deviations for substances from different chemical families. The general applicability of the corresponding states principle to the Mie fluid has been confirmed by *Orea et al.*[18,59] and *Galliero et al.*[16] for different vapor-liquid equilibrium properties. *Jaramillo-Gutierrez et al.* have studied the thermodynamic geometry of the Mie fluid finding that the corresponding states principle can be reasonably well applied at moderate pressures and temperatures[26]. The applicability of the corresponding states principle at extreme conditions has to the best of our knowledge not yet been tested for the Mie fluid.

In this work, we applied the method of *Urschel & Stephan*[35] for determining the characteristic curves of the Mie n, m fluid. Thereby, the influence of the Mie potential exponents n and m on the characteristic curves is elucidated and insight into the extrapolation behavior of the Mie fluid is obtained. Moreover, the applicability of the corresponding states principle[57,58] is tested based on the characteristic curve results of the different Mie fluids. For determining the critical point of the Mie fluids, VLE Grand Equilibrium[60] simulations were additionally carried out.

This work is structured as follows: First, the simulation method and computational details are introduced in section II. Then, the results for the characteristic curves and the influence of the exponents are discussed in section III. Finally, the applicability of the corresponding states principle on the Mie fluid at extreme conditions is assessed.

II. METHODS

In this work, the approach proposed by *Urschel & Stephan* for determining Brown's characteristic curves[35] was applied. In this approach, three main aspects are combined: (i) using an equation of state for estimating the location of the curves; (ii) carrying out molecular dynamics simulations; and (iii) computing the state points of the characteristic curves in the limit $\rho \to 0$ via the second virial coefficient by direct integration of the interaction potential[35].

In this work, we used the molecular-based equation of state proposed by *Lafitte et al.*[6], which describes the thermodynamic properties of the Mie fluid. As described in Ref.[35], the equation of state initial guess values for the characteristic curves were corrected by exact results computed via the virial coefficient route in the zero-density limit. This correction was only applied for the initial guess values used for the molecular simulations. In the results section, the original equation of state results are presented and discussed.

The second virial coefficient $\tilde{B}$ was computed directly from the intermolecular potential $u_{\mathrm{Mie}}(r)$ as[61,62]

$$\tilde{B} = -\frac{1}{2V} \iint f_{12} \, \mathrm{d}\mathbf{r}_1 \mathrm{d}\mathbf{r}_2 \,, \tag{2}$$

where f indicates the Mayer function

$$f = \exp\left(-u_{\mathrm{Mie}}(r)/T\right) - 1 \,, \tag{3}$$

and r indicates the distance between two interacting particles[62]. In Eq. 2, a volume element in which the particle is located is indicated by $\mathrm{d}\mathbf{r}$. Eq. (2) can be integrated numerically, cf. Ref.[62,63]. Eqs. (2) and (3) were implemented and integrated (using a semi-infinite integration range, cf. Ref.[64]). Thereby, practically exact results for $\tilde{B}(T)$ were obtained. From the results for $\tilde{B}(T)$, specific conditions yield the zero-density limit state points of the characteristic curves[30]. Therefore, no statistical uncertainty applies to the zero-density limit data points of the characteristic curves (in contrast to the molecular simulation results).

For the molecular simulations, the software package $ms2$ was used[65,66]. For determining the four characteristic curves in the molecular simulations, the thermodynamic conditions were applied that were found to be most favorable, cf. Ref.[35]. For determining a state point on the Zeno curve, sets of NVT simulations along an isotherm in the vicinity of the initial guess value were carried out and evaluated using the thermodynamic condition $Z = 1$. Also for the Boyle and Charles curve, sets of NVT simulations along isotherms were carried out. For the Boyle curve, the thermodynamic condition $(\partial Z/\partial V)_T = 0$ was evaluated. For the Charles curve, the thermodynamic condition $(\partial H/\partial p)_T = 0$ was evaluated. For the Amagat curve, sets of NpT simulations along an isotherm were carried out and the condition $(\partial U/\partial V)_T = 0$ was applied. For all four characteristic curves, around 20 state points on a characteristic curve were determined. For each characteristic curve state point, a set of seven MD simulations was considered. The results from each set of simulations were evaluated

by fitting a second order polynomial and evaluating that function regarding the respective thermodynamic condition (see above). Finally, for each state point determined for the characteristic curves, an additional NVT simulation was carried out to determine further thermodynamic properties. In particular, the *Lustig* formalism[66–68] was applied for these simulations, which gives direct access to the Helmholtz energy derivatives. Using that data, the characteristic curve state points were evaluated regarding thermodynamic consistency[35]. The statistical uncertainties of the determined characteristic curve state points were estimated using error propagation, cf. Ref.[35] for details. The data set for a given characteristic fluid was complemented by the respective exact zero-density limit state point obtained from the virial route.

The time step used in the MD simulations was $\Delta\tau = 0.001\,\sigma\sqrt{M/\varepsilon}$. The treatment of the long-range interactions have an important influence on the virial coefficient[69], liquid bulk phase properties[70] as well as phase equilibrium properties[71]. Here, the cut-off radius was set to 5σ in combination with classical long-range corrections for bulk properties such as the internal energy and the pressure[66,72]. For the NVT simulations, systems with 2,500 particles were studied. The systems were equilibrated for 50,000 time steps and production was carried out for 750,000 time steps. For the NpT simulations, an additional equilibration time of 50,000 time steps was applied. Classical velocity scaling was used for prescribing the temperature. For prescribing the pressure, Andersen's barostat was used. The piston mass of the barostat was specified depending on the state point based on the heuristic approach proposed in Ref.[35].

In addition to the characteristic curve MD simulations, VLE simulations were carried out to obtain data on the critical parameters of the Mie fluids for the evaluation of the corresponding states principle. The VLE simulations were carried out using the Grand Equilibrium method of *Vrabec and Hasse*[60]. Simulation details are given in the Supplementary Material. The thermodynamic consistency of the VLE data was furthermore assessed using the compressibility factor test proposed by *Nezbeda*[73].

In total, 14 Mie fluids were studied. For the variation of the repulsive exponent, 10 Mie fluids were considered with $n = 8, 10, 11, 12, 13, 14, 16, 20, 36, 48$. For these fluids, the dispersive exponent was kept constant at $m = 6$. For the variation of the dispersive exponent, $m = 4, 5, 6, 7, 8$ were studied and the repulsive exponent was constant at $n = 12$. The results for the Mie fluids 11, 6 and 13, 6 are only presented in the electronic Supplementary Material.

III. RESULTS

The results section is outlined as follows: First, the results for the second virial coefficient and its characteristic points (cf. Fig. 2-bottom) are presented and discussed. Then, the results for the characteristic curves of the Mie $n, 6$ and $12, m$ fluid are discussed. Finally, the results of the characteristic curves are used to assess the applicability of the corresponding states principle at extreme conditions. Numerical data are given in the Supplementary Material. Also, the results for the VLE of the Mie fluids are discussed in detail in the Supplementary Material.

A. Virial Coefficient

Fig. 3 shows the results for the second virial coefficient as a function of the temperature. Fig. 3-top shows the results for the variation of the repulsive exponent n; Fig. 3-bottom those for the variation of the dispersive exponent m. The second virial coefficient results from this work are in agreement with those reported by $Sadus$[21] (for special n, m combinations). Fig. 4 shows the results for the characteristic points of the second virial coefficient, i.e. $\tilde{B} = 0$, $(\partial \tilde{B}/\partial T) = \tilde{B}/T$, and $\tilde{B} = \tilde{B}_{\max}$, which correspond to the zero-density limit temperatures of the characteristic curves.

Overall, both exponents have an important influence on the behavior of the second virial coefficient of the Mie fluid. For high temperatures (and $\tilde{B} > 0$), where the repulsive interactions dominate the fluid behavior since the mean energy of the particles exceeds the dispersion energy ε, the repulsive exponent n has a strong influence on the virial coefficient. On the other hand, as the dispersive interactions dominate at low temperatures (and $\tilde{B} < 0$) and the total energy of the particles is on the order of magnitude of the dispersion energy ε, the attractive exponent m has a strong influence on the virial coefficient in that region.

Interestingly, a complex influence is observed for the repulsive exponent: The maximum of the second virial coefficient, i.e. the zero-density limit of the Amagat curve (cf. Fig. 2), first decreases with increasing n, reaches a temperature minimum and then increases with increasing n. The two underlying counter-acting effects are due to the fact that the repulsive exponent n influences the shape of the potential in both the repulsive and attractive part, cf. Fig. 1-left. The dispersive exponent m on the other hand influences primarily the shape
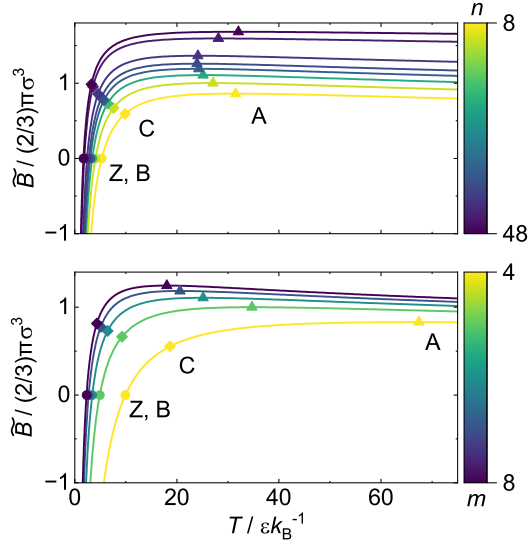
9

FIG. 3: Second virial coefficient $\tilde{B}$ of the Mie n,6 fluid (top) and Mie 12,m fluid (bottom) as a function of the temperature. Results from numerical integration of the interaction potential (cf. Eqs. 2 and 3). Characteristic points are indicated by different symbols: Bullets (Z, B) indicate $\tilde{B} = 0$, diamonds (C) indicate $(\partial \tilde{B}/\partial T) = \tilde{B}/T$, and triangles (A) indicate $\tilde{B} = \tilde{B}_{\text{max}}$. The characteristic points are related to Brown's characteristic curves as shown in Fig. 2.

of the attractive part of the potential (cf. Fig. 1-right), which corresponds to the fact that m influences the second virial coefficient and its characteristic points in a monotonous way, cf. Figs. 3 and 4.

Also the overall influence of the potential parameters n and m on the virial coefficient $\tilde{B}$ can be well understood from the inspection of the shape of the potential, cf. Fig. 1. The interaction range of the potential decreases with increasing m. Therefore, with increasing m, the virial coefficient curves $\tilde{B}(T)$ are shifted to higher temperatures and become more flat – especially in the low-temperature range. For large m values, the particles exhibit stronger attractive forces $\mathbf{f} = \mathrm{d}u_{\text{Mie}}/\mathrm{d}\mathbf{r}$, but in a smaller distance range compared to small m values. Hence, particles that come into the attractive interaction range at high m, have a higher probability to stick together compared to low m values. This is reflected in the shift of $\tilde{B}$ with increasing m. Interestingly, the same effect – but less prominent – is observed for increasing n, cf. Fig. 3-top. This is due to the fact that the attractive part of the interaction potential to some extend also changes upon increasing n, cf. Fig. 1-left.

For the Boyle (B) and Charles (C) zero-density limit characteristic points, increasing n
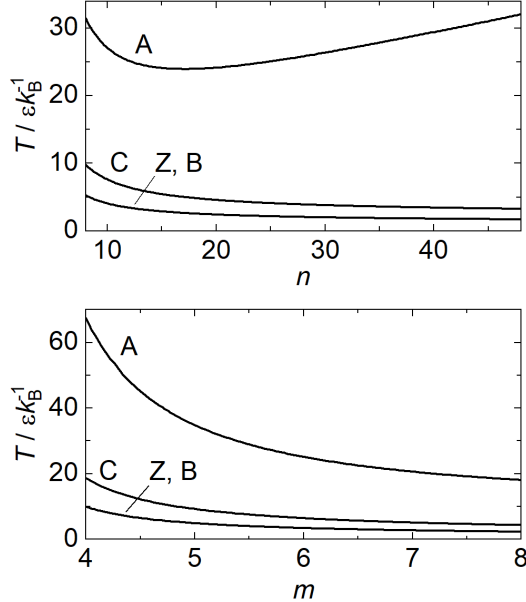
FIG. 4: Characteristic points Z, A, B, and C of the second virial coefficient (cf. Fig. 3) as function of the repulsive exponent n (top) and the dispersive exponent m (bottom). Results from numerical integration of the interaction potential (cf. Eqs. 2 and 3).

yields decreasing characteristic temperatures. The temperature minimum of the Amagat curve is determined here to be at $n_{\min} = 17.1$. For the dispersive exponent, all three characteristic temperatures decrease with increasing m, cf. Fig. 4-bottom. A comparison of characteristic points of $\tilde{B}(T)$ predicted by the EOS and the exact values for the studied Mie fluids is given in Supplementary Material. The deviations between those two data sets are small in most cases. Nevertheless, the simulation method[35] used for determining the characteristic curves considers the exact values, i.e. the EOS initial guess values for the characteristic curves were corrected by the exact zero-density limit values, cf. Ref.[35] for details.

B. Characteristic Curves

Fig. 5 shows the results for all four characteristic curves of the $n, 6$ Mie fluids; Fig. 6 shows the results for the $12, m$ Mie fluids. The results for the four curves are depicted in both the pressure-temperature projection and the density-temperature projection. Both, the simulation results and the EOS predictions for the characteristic curves are shown. Also,

the VLE simulation and EOS results are shown (with a 50% transparency) in Figs. 5 and 6.

In all cases, the simulation results for the characteristic curves show a smooth trend. Also, the MD simulation results (circles) are in excellent agreement with the exact results for the zero-density data points (triangles) obtained from the virial route. In practically all cases, the statistical uncertainties of the MD results are within the symbol size. For the Zeno and the Amagat curve, simulations were carried out until solidification was observed in the simulations. For the Boyle curve, simulations were successfully carried out also in the vapor-liquid metastable region that are consistent with the predictions from the EOS[6] (details are shown in the Supplementary Material). The thermodynamic consistency of the simulation results is moreover confirmed by the evaluation of the Helmholtz energy derivative characteristic curve criteria[35]. The results of that test are presented in the Supplementary Material. For the vast majority of data points, the results for the Helmholtz energy derivatives are in accordance with the respective condition. All this confirms the robustness of the method proposed in Ref.[35].

The predictions of the Mie equation of state of *Lafitte et al.*[6] are overall in good agreement with the computer experiment results from this work (cf. Figs. 5 and 6). The absolute average deviation for the $n, 6$ Mie fluids are 8.5% for the pressure and 6.1% for the density and for the $12, m$ Mie fluids 10.7% for the pressure and 8.2% for the density. This is astonishing considering the fact that the characteristic curves cover a large range of states and the fact that the model of *Lafitte et al.* was not trained to such data. This indicates that the molecular-based formulation of that model is very robust. The model of *Lafitte et al.* also covers the anomaly behavior of the zero-density limit of the Amagat curve, i.e. it exhibits a temperature minimum at $n_{\min}$. Only, for very small dispersive exponents $m < 5$, the equation of state of *Lafitte et al.* yields spurious Amagat curves, cf. Fig. 6. This is not surprising as this is also out of the range of validity stated by *Lafitte et al.*[6].

The results for the influence of the repulsive exponent on the macroscopic thermodynamic properties yields several insights. The variation of the repulsive exponent n has a similar effect on the Zeno, Charles, and Boyle curve (cf. Fig. 5): Their pressure and temperature range increases with decreasing n, i.e. increasing softness of the potential. For the Amagat curve, a more complex behavior is obtained: At low temperatures, the pressure of the Amagat curve increases monotonously with increasing n. At high temperatures, however, the pressure of the Amagat curve first decreases and then increases with increasing n. This

is a result of the minimum of the zero-density limit Amagat temperature T_A, cf. Fig. 4, and the fact that competing effects are present regarding the molecular interactions. Moreover, important differences are observed for the Amagat curve in comparison to the other three curves in the density-temperature projection: For the Zeno, Charles, and Boyle curve, the repulsive exponent has an important influence. In the studied n-range, the Zeno, Charles, and Boyle curve exhibit a significant shift to higher temperatures. The behavior of the Amagat curves in the density-temperature projection on the other hand is only slightly affected by the repulsive exponent n.

The characteristic curves are closely related to the VLE, e.g. the Boyle and the Charles curve originate on the spinodal and binodal, respectively. The VLE results for the Mie fluids are presented and discussed in detail in the Supplementary Material. The MD VLE results are consistent with the compressibility factor rule proposed by *Nezbeda*[73]. Moreover, the VLE results obtained from the EOS of *Lafitte et al.*[6] are in reasonable agreement with the computer experiment results (see Supplementary Material for details). Both Mie potential exponents influence the VLE properties: The vapor pressure and the critical temperature are strongly influenced by both the repulsive and the dispersive exponent. The exponent n has only a minor influence on the saturated densities as well as the critical density. This is as expected, as the particle size, i.e. the intermolecular distance r at which the repulsive interactions occur, are hardly affected by n and m, cf. Fig. 1. Overall, the repulsive and dispersive exponent have similar effects on the VLE properties, which is likely due to the fact that the attractive interactions play a dominant role in establishing a stable liquid phase. Both interaction exponents widen the range of attractive interactions with decreasing n and m, cf. Fig. 1, which increases the mean dispersive interactions at a given density. Therefore, a stable liquid phase can be established at higher temperatures for low n and m.

The differences for the influence of n and m on the different VLE properties, i.e. saturated densities and vapor pressure, are also reflected on the characteristic curves. Accordingly, the density behavior of the characteristic curves is only slightly influenced by n and m and the high-density limit for a given characteristic curves is similar for the different Mie fluids. For the Zeno curve, all Mie $n, 6$ fluids converge to a common line at low temperatures in the pressure-temperature projection and have approximately a common intersection point in the vicinity of the triple point liquid phase density in the density-temperature projection (cf. Fig. 5 b). For the Boyle curves, the termination on the spinodal has the same behavior

13

as that of the critical point density for varying n and m (cf. Fig. 5 f). The same holds for the Charles curves (cf. Fig. 5 h). Only for the Amagat curves, (cf. Fig. 5 d), a more complex density dependency is observed upon a variation of n.

The variation of the attractive exponent m has the same qualitative effect on all four characteristic curves: The pressure and temperature increases with increasing m. This is opposite to the influence of the repulsive exponent n, which affects the Amagat curve differently than the other three characteristic curves. For the Amagat curve, the variation of the repulsive exponent n has multiple effects that superimpose in a complex way (cf. Fig. 5 c), which is likely due to the fact that n affects both the repulsive and the dispersive part of the potential (cf. Fig. 1).

While the exponents n and m have the same qualitative influence on the characteristic curves (except the Amagat curve), the comparison of the results for the influence of n and those of m (Figs. 5 and 6) reveals important quantitative differences: The attractive exponent m has a significantly stronger influence on the characteristic curves than n – in particular in the pressure-temperature projection. While the value for m was varied only in the range 4..8 compared to the variation of $n = 8..48$, the pressure maximum is influenced more strongly for a given characteristic curve by m. This is surprising as it shows that attractive interactions still play an important role also at extreme pressure and temperature.

For all studied $n, 6$ and $12, m$ Mie fluids, the Zeno curve exhibits approximately a linear trend in the density-temperature plane. This phenomenon has been discussed in detail by *Apfelbaum* and co-workers for different molecular fluids (both model and real substance fluids)[27,45,46]. In fact, the results from this work show that also the three 1st-order characteristic curves (Amagat, Boyle, and Charles) exhibit an approximately linear trend in the density-temperature projection, however, with a slightly convex shape at low temperature in most cases, cf. Figs. 5 and 6.
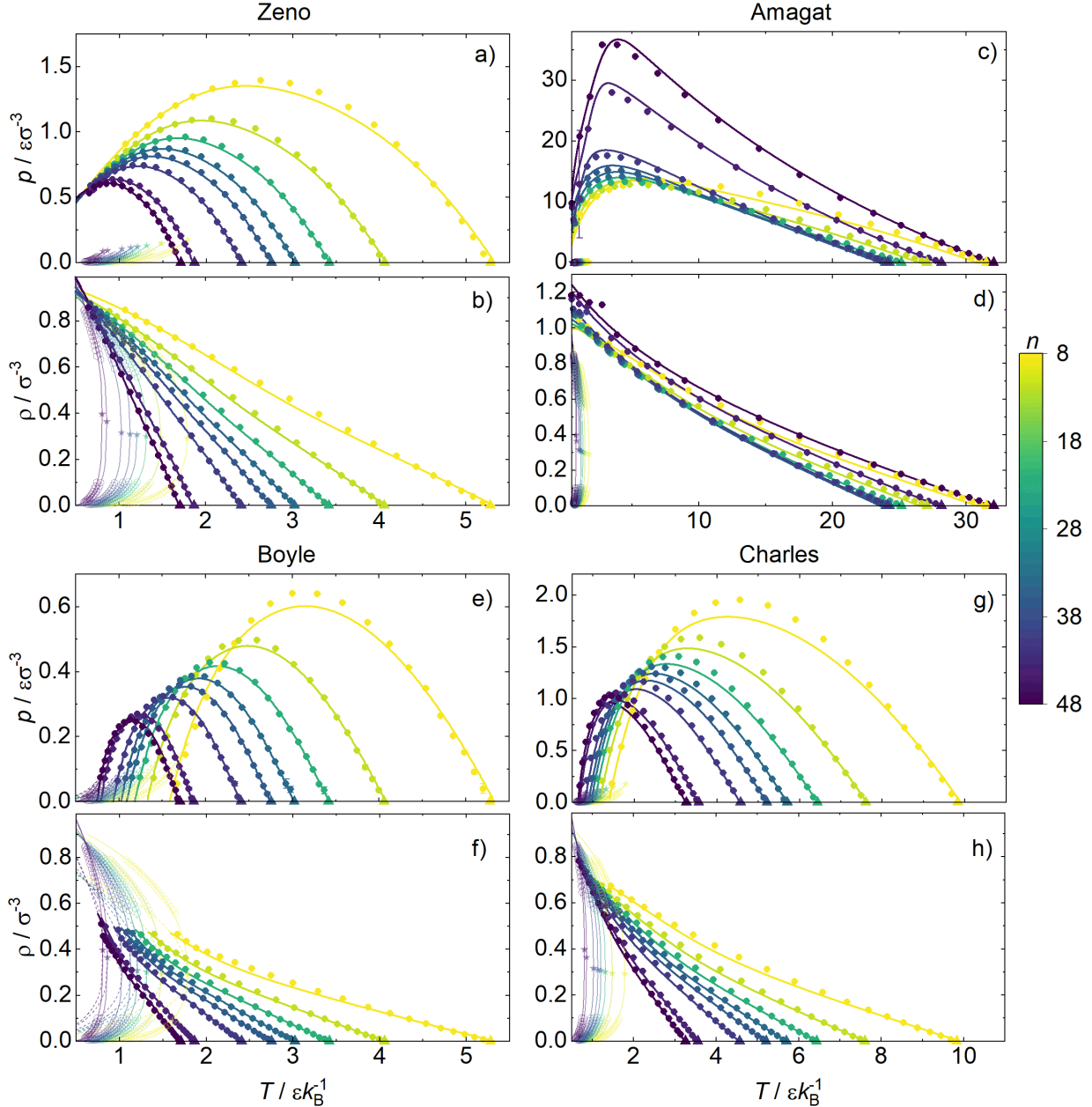
FIG. 5: Characteristic curves of Mie n, 6 fluid: a) and b) Zeno curve; c) and d) Amagat curve; e) and f) Boyle curve; g) and h) Charles curve. For each curve, results are presented in the p-T and ρ-T projection. The repulsive exponent is represented by the color code. Results from MD (filled and open circles) and the EOS[6] (lines and star). Statistical uncertainties for characteristic curve MD data are within the symbol size. Top triangles indicate zero-density limit characteristic points computed via the virial route (cf. Fig. 2-bottom). The 50% transparent lines and symbols indicate the vapor-liquid equilibrium (solid lines indicate binodal; dashed lines indicate spinodal; star indicates critical point). Open circles indicate VLE results obtained from MD simulations.
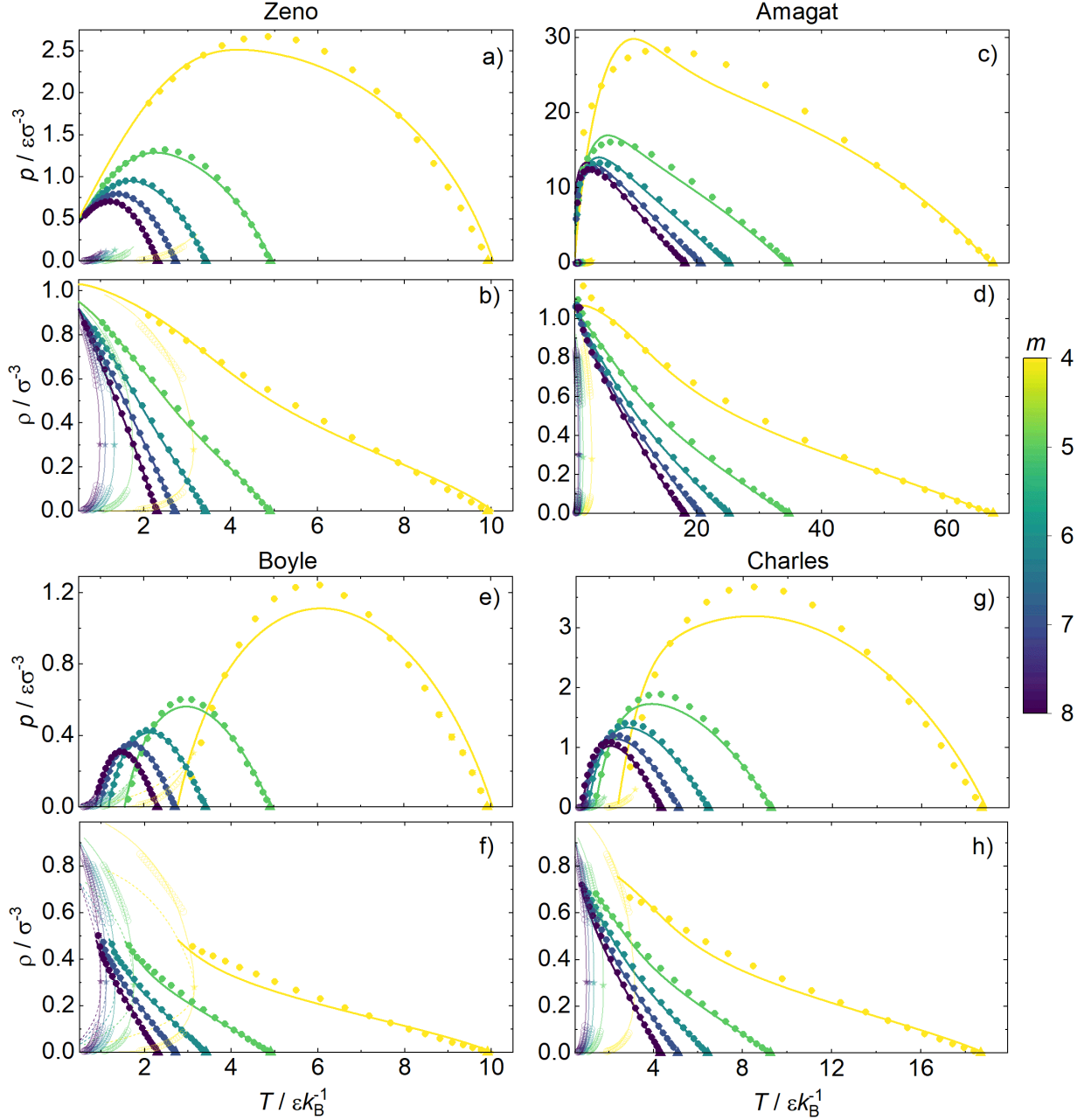
FIG. 6: Characteristic curves of Mie 12, m fluid: a) and b) Zeno curve; c) and d) Amagat curve; e) and f) Boyle curve; g) and h) Charles curve. For each curve, results are presented in the p-T and ρ-T projection. The repulsive exponent is represented by the color code. Results from MD (filled and open circles) and the EOS[6] (lines and star). Statistical uncertainties for characteristic curve MD data are within the symbol size. Top triangles indicate zero-density limit characteristic points computed via the virial route (cf. Fig. 2-bottom). The 50% transparent lines and symbols indicate the vapor-liquid equilibrium (solid lines indicate binodal; dashed lines indicate spinodal; star indicates critical point). Open circles indicate VLE results obtained from MD simulations.

C.   Corresponding States Principle

Fig. 7 shows the MD results for the characteristic curves of the Mie fluid in reduced units with respect to the critical parameters. Based on these results, the applicability of the classical corresponding states principle at extreme conditions is assessed. Table I summarizes characteristic points of the characteristic curves in reduced units. The critical parameters were determined from the MD VLE simulation data obtained in this work (see Supplementary Material for details).

Following the corresponding states principle, the results for the different Mie fluids should collapse on a master curve when plotted in reduced units. Interestingly, important deviations from the corresponding states principle are observed – in particular for the variation of the repulsive exponent and at high temperatures, cf. Fig. 7-top. At high temperatures, the reduced temperature of all four characteristic curves is shifted. For the Zeno, Boyle, and Charles curve, the results for the different Mie fluids are shifted to higher reduced temperatures with increasing n. For the Amagat curve, on the other hand, the reduced temperature decreases with increasing n in the high temperature region. Hence, the Amagat and the Charles curve approach each other with increasing n. The reduced pressure follows the corresponding states principle relatively well for the Zeno, Boyle, and Charles curve, whereas significant deviations from the corresponding states principle are observed for the Amagat curve reduced pressure, which varies about an order of magnitude in the studied n-range.

For the Zeno, Boyle, and Charles curve, the corresponding states principle is very well satisfied at low temperatures – for both varying n and varying m. Deviations appear with increasing temperature in the vicinity of the pressure maximum of the respective curve.

Interestingly, the Amagat curve follows the corresponding states principle relatively well for the variation of m (cf. Fig. 7-bottom). For the Zeno, Boyle, and Charles curve, the two exponents have a similar influence on the deviations of the corresponding states principle, i.e. the reduced temperature increases with increasing exponent n and m at high temperatures, whereas the reduced pressure is in good accordance with the corresponding states principle.

TABLE I: Characteristic points of Brown's characteristic curves for the Mie n, 6 and Mie 12, m fluid in terms of reduced temperature $T^* = T/T_c$ and reduced pressure $p^* = p/p_c$. For each curve, the pressure and temperature of the pressure maximum $p_{max}(T)$ and the temperature of the zero-density limit are reported. The pressure maximum data was computed from MD results by spline interpolation. The zero-density limit data was computed via the virial route. Critical point parameters were taken from the MD data.

|	Zeno		Amagat		Boyle		Charles	
	p_{max}	$\lim_{\rho \to 0}$	p_{max}	$\lim_{\rho \to 0}$	p_{max}	$\lim_{\rho \to 0}$	p_{max}	$\lim_{\rho \to 0}$
n,m	T^*/p^*	T^*	T^*/p^*	T^*	T^*/p^*	T^*	T^*/p^*	T^*
8,6	1.49/8.78	2.97	4.03/84.30	17.73	1.76/4.06	2.97	2.52/12.32	5.53
10,6	1.39/8.41	2.77	3.73/97.99	18.48	1.71/3.82	2.77	2.33/12.14	5.19
12,6	1.34/8.16	2.64	3.49/112.73	19.40	1.63/3.65	2.64	2.25/12.01	4.96
14,6	1.27/7.86	2.54	3.21/126.98	20.40	1.60/3.49	2.54	2.13/11.77	4.79
16,6	1.28/7.86	2.47	3.17/145.91	21.46	1.54/3.45	2.47	2.10/11.97	4.66
20,6	1.21/7.66	2.36	3.16/180.60	23.69	1.52/3.34	2.36	2.02/12.06	4.49
36,6	1.11/7.46	2.19	3.52/331.35	33.09	1.44/3.15	2.19	1.84/12.38	4.18
48,6	1.12/7.36	2.14	4.03/449.67	40.21	1.42/3.07	2.14	1.81/12.50	4.09
12,4	1.53/9.45	3.13	4.54/100.39	21.27	1.86/4.41	3.13	2.68/13.03	5.89
12,5	1.41/8.49	2.82	3.84/103.38	19.97	1.71/3.89	2.82	2.39/12.16	5.32
12,6	1.34/8.16	2.64	3.49/112.73	19.40	1.63/3.65	2.64	2.25/12.01	4.96
12,7	1.29/7.91	2.50	3.06/123.64	19.02	1.59/3.50	2.50	2.13/11.94	4.70
12,8	1.24/7.70	2.40	1.17/150.92	18.79	1.54/3.37	2.40	2.09/11.94	4.49
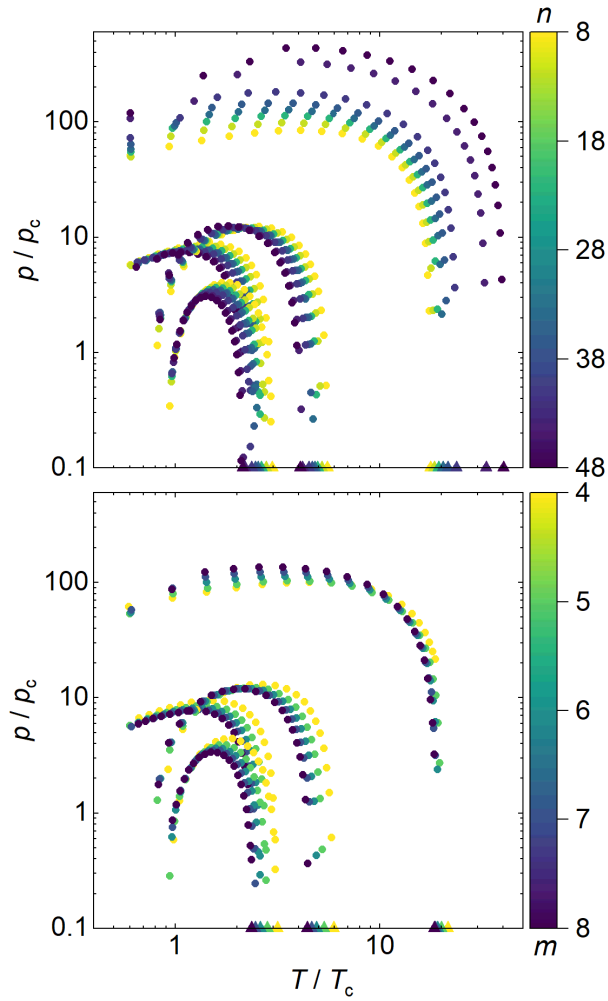
FIG. 7: Characteristic curves of Mie n, 6 fluid (top) and Mie 12, m fluid (bottom) in the double-logarithmic pressure-temperature projection. All results are reduced with the critical parameters. Circles indicate MD results; triangles indicate the zero-density limit results obtained from the virial route. Critical point parameters T_c and p_c were taken from the MD data (see Supplementary Material).

IV. CONCLUSIONS

In this work, Brown's characteristic curves of the Mie fluid were investigated to elucidate the relation of the shape of the intermolecular potential of a simple fluid and macroscopic thermodynamic properties at extreme conditions. Therefore, molecular dynamics simulations were carried out to determine state points of the 0th and 1st-order characteristic curves of the $n, 6$ and $12, m$ Mie fluid. The results were moreover used to assess the applicability of the corresponding states principle. Interestingly, large deviations from the corresponding states principles were found – in particular caused by the variation of the repulsive exponent of the Mie potential. Furthermore, a complex and anomalous behavior of the Amagat curve of the $n, 6$ Mie fluid was elucidated: While the Zeno, Boyle, and Charles curve show a simple dependency on the exponent n (and the exponent m), the Amagat curve exhibits a complex behavior upon a variation of the repulsive exponent n. This is attributed to the fact that the variation of the repulsive exponent n has different effects on the shape of the intermolecular potential. Interestingly, this anomalous behavior is qualitatively captured by the corresponding states principle, i.e. a simple monotonous dependency is obtained for the Amagat curve as a function of n in reduced units T/T_{c} and p/p_{c}, which is due to the dependency $T_{\text{c}}(n)$ and $p_{\text{c}}(n)$.

Overall, the Mie potential exponents n and m strongly influence the temperature and pressure behavior, whereas only a minor effect is observed on the density. This is consistently found for the characteristic curves as well as for the vapor-liquid equilibrium.

The results from this work stress the fact the both exponents actually affect the intermolecular potential in the entire distance range to some extend. This is supported from the results for the characteristic curves and their zero-density limit (computed from the virial coefficient) as well as for the vapor-liquid equilibrium.

The comprehensive characteristic curve data for the Mie fluid from this work can be favorably used for the development and testing of new Mie equations of state[74]. Thereby, the thermodynamic consistency and extrapolation capabilities can be assessed.

ACKNOWLEDGMENTS

CONFLICTS OF INTEREST

There are no conflicts of interest to declare.

REFERENCES

[1] E. A. Müller and G. Jackson, "Force-field parameters from the SAFT-γ equation of state for use in coarse-grained molecular simulations," Annual Review of Chemical and Biomolecular Engineering **5**, 405–427 (2014).

[2] J. J. Potoff and G. Kamath, "Mie potentials for phase equilibria: Application to alkenes," Journal of Chemical & Engineering Data **59**, 3144–3150 (2014).

[3] J. J. Potoff and D. A. Bernard-Brunel, "Mie potentials for phase equilibria calculations: Application to alkanes and perfluoroalkanes," The Journal of Physical Chemistry B **113**, 14725–14731 (2009).

[4] S. Stephan, M. Horsch, J. Vrabec, and H. Hasse, "MolMod - an open access database of force fields for molecular simulations of fluids," Molecular Simulation **45**, 806–814 (2019).

[5] S. Schmitt, F. Fleckenstein, H. Hasse, and S. Stephan, "Comparison of force fields for the prediction of thermophysical properties of long linear and branched alkanes," The Journal of Physical Chemistry B **127**, 1789–1802 (2023).

[6] T. Lafitte, A. Apostolakou, C. Avendano, A. Galindo, C. S. Adjiman, E. A. Müller, and G. Jackson, "Accurate statistical associating fluid theory for chain molecules formed from Mie segments," The Journal of Chemical Physics **139**, 154504 (2013).

[7] H. Guérin, "Simple analytic equations of state for the generalized hard-core mie(α, β) and mie(α, β) fluids from perturbation theory," Journal of Molecular Liquids **164**, 162–170 (2011).

[8] G. Mie, "Zur kinetischen Theorie der einatomigen Körper," Annalen der Physik **316**, 657–697 (1903).

[9] E. Grüneisen, "Das Verhältnis der thermischen Ausdehnung zur spezifischen Wärme fester Elemente," Zeitschrift für Elektrochemie und angewandte physikalische Chemie **17**, 737–739 (1911).

[10] M. N. Rosenbluth and A. W. Rosenbluth, "Further results on Monte Carlo equations of state," The Journal of Chemical Physics **22**, 881–884 (1954).

[11] W. W. Wood and F. R. Parker, "Monte Carlo equation of state of molecules interacting with the Lennard-Jones potential. I. A supercritical isotherm at about twice the critical temperature," The Journal of Chemical Physics **27**, 720–733 (1957).

[12] S. Stephan, M. Thol, J. Vrabec, and H. Hasse, "Thermophysical properties of the Lennard-Jones fluid: Database and data assessment," Journal of Chemical Information and Modeling **59**, 4248–4265 (2019).

[13] S. Stephan, J. Staubach, and H. Hasse, "Review and comparison of equations of state for the Lennard-Jones fluid," Fluid Phase Equilibria **523**, 112772 (2020).

[14] A. J. Stone, *The Theory of Intermolecular Forces*, 2nd ed. (Oxford University Press, Oxford, 2016).

[15] S. Werth, K. Stöbener, M. Horsch, and H. Hasse, "Simultaneous description of bulk and interfacial properties of fluids by the Mie potential," Molecular Physics **115**, 1017–1030 (2017).

[16] G. Galliero, M. M. Piñeiro, B. Mendiboure, C. Miqueu, T. Lafitte, and D. Bessieres, "Interfacial properties of the Mie n-6 fluid: Molecular simulations and gradient theory results," The Journal of Chemical Physics **130**, 104704 (2009).

[17] J. Janeček, O. Said-Aizpuru, and P. Paricaud, "Long range corrections for inhomogeneous simulations of Mie n-m potential," Journal of Chemical Theory and Computation **13**, 4482–4491 (2017).

[18] P. Orea, Y. Reyes-Mercado, and Y. Duda, "Some universal trends of the Mie(n,m) fluid thermodynamics," Physics Letters A **372**, 7024–7027.

[19] H. Okumura and F. Yonezawa, "Liquid-vapor coexistence curves of several interatomic model potentials," The Journal of Chemical Physics **113**, 9162–9168 (2000).

[20] A. Ahmed and R. J. Sadus, "Solid-liquid equilibria and triple points of n-6 Lennard-Jones fluids," The Journal of Chemical Physics **131**, 174504 (2009).

[21] R. J. Sadus, "Intermolecular potential-based equations of state from molecular simulation and second virial coefficient properties," The Journal of Physical Chemistry B **122**, 7757–7763 (2018).

[22] D. M. Heyes, G. Rickayzen, S. Pieprzyk, and A. C. Brańka, "The second virial coefficient and critical point behavior of the Mie potential," The Journal of Chemical Physics **145**, 084505 (2016).

[23] J. Mairhofer and R. J. Sadus, "Thermodynamic properties of supercritical n-m Lennard-Jones fluids and isochoric and isobaric heat capacity maxima and minima," The Journal of Chemical Physics **139**, 154503 (2013).

[24]G. Galliero, T. Lafitte, D. Bessieres, and C. Boned, "Thermodynamic properties of the Mie n-6 fluid: A comparison between statistical associating fluid theory of variable range approach and molecular dynamics results," The Journal of Chemical Physics **127**, 184506 (2007).

[25]A. E. Nasrabad, R. Laghaei, and B. C. Eu, "Molecular theory of thermal conductivity of the Lennard-Jones fluid," The Journal of Chemical Physics **124**, 084506 (2006).

[26]J. Jaramillo-Gutiérrez, J. López-Picón, and J. Torres-Arenas, "Subcritical and supercritical thermodynamic geometry of Mie fluids," Journal of Molecular Liquids **347**, 118395 (2022).

[27]E. M. Apfelbaum and V. S. Vorob'ev, "The confirmation of the critical point-zeno-line similarity set from the numerical modeling data for different interatomic potentials," The Journal of Chemical Physics **130**, 214111 (2009).

[28]E. H. Brown, "On the thermodynamic properties of fluids," Bulletin de l'Institut International du Froid **1960-1**, 169–178 (1960).

[29]R. Span, *Multiparameter Equations of State* (Springer, Berlin, 2000).

[30]S. Stephan and U. K. Deiters, "Characteristic curves of the Lennard-Jones fluid," International Journal of Thermophysics **41**, 147 (2020).

[31]N. M. Alsaifi and J. R. Elliott, "Avoiding artifacts in noncubic equations of state," Industrial & Engineering Chemistry Research **61**, 15661–15677 (2022).

[32]R. Span and W. Wagner, "On the extrapolation behavior of empirical equations of state," International Journal of Thermophysics **18**, 1415–1443 (1997).

[33]U. K. Deiters and K. M. De Reuck, "Guidelines for publication of equations of state – I. pure fluids," Chemical Engineering Journal **69**, 69–81 (1998).

[34]O. L. Boshkova and U. K. Deiters, "Soft repulsion and the behavior of equations of state at high pressures," International Journal of Thermophysics **31**, 227–252 (2010).

[35]M. Urschel and S. Stephan, "Determining Brown's characteristic curves using molecular simulation," Journal of Chemical Theory and Computation **5**, 1537–1552 (2023).

[36]A. Neumaier and U. K. Deiters, "The characteristic curves of water," International Journal of Thermophysics **37**, 96 (2016).

[37]U. K. Deiters and A. Neumaier, "Computer simulation of the characteristic curves of pure fluids," J. Chem. Eng. Data. **61**, 2720–2728 (2016).

[38]E. Holleran, "The intersection of the inversion curve and the unit compressibility line," Industrial & Engineering Chemistry Fundamentals **13**, 297–298 (1974).

[39] J. Vrabec, G. K. Kedia, and H. Hasse, "Prediction of Joule-Thomson inversion curves for pure fluids and one mixture by molecular simulation," Cryogenics **45**, 253–258 (2005).

[40] J. Vrabec, A. Kumar, and H. Hasse, "Joule-Thomson inversion curves of mixtures by molecular simulation in comparison to advanced equations of state: Natural gas as an example," Fluid Phase Equilibria **258**, 34–40 (2007).

[41] A. Pakravesh and H. Zarei, "Prediction of Joule-Thomson coefficients and inversion curves of natural gas by various equations of state," Cryogenics **118**, 103350 (2021).

[42] S. Stephan, M. Dyga, H. Urbassek, and H. Hasse, "The influence of lubrication and the solid-fluid interaction on thermodynamic properties in a nanoscopic scratching process," Langmuir **35**, 16948–16960 (2019).

[43] S. Stephan, S. Schmitt, H. Hasse, and H. M. Urbassek, "Molecular dynamics simulation of the Stribeck curve: Boundary lubrication, mixed lubrication, and hydrodynamic lubrication on the atomistic level," Friction , in press.

[44] D. W. Green and M. Z. Southard, *Perry's chemical engineers' handbook*, 9th ed. (McGraw-Hill Education, New York, 2019).

[45] E. M. Apfelbaum, V. S. Vorob'ev, and G. A. Martynov, "Triangle of liquid-gas states," The Journal of Physical Chemistry B **110**, 8474–8480 (2006).

[46] E. M. Apfelbaum, V. S. Vorob'ev, and G. A. Martynov, "Regarding the theory of the Zeno line," The Journal of Physical Chemistry A **112**, 6042–6044 (2008).

[47] E. M. Apfelbaum and V. S. Vorob'ev, "The similarity law for the Joule–Thomson inversion line," The Journal of Physical Chemistry B **118**, 12239–12242 (2014).

[48] E. M. Apfelbaum and V. S. Vorob'ev, "Similarity laws for the lines of ideal free energy and chemical potential in supercritical fluids," The Journal of Physical Chemistry B **121**, 8802–8808 (2017).

[49] J. Rößler, I. Antolovic, S. Stephan, and J. Vrabec, "Assessment of thermodynamic models via Joule-Thomson inversion," Fluid Phase Equilibria **556**, 113401 (2022).

[50] C. G. Aimoli, E. J. Maginn, and C. R. A. Abreu, "Thermodynamic properties of supercritical mixtures of carbon dioxide and methane: A molecular simulation study," Journal of Chemical & Engineering Data **59**, 3041–3054 (2014).

[51] S. Figueroa-Gerstenmaier, M. Lísal, I. Nezbeda, W. R. Smith, and V. M. Trejos, "Prediction of isoenthalps, Joule-Thomson coefficients and Joule-Thomson inversion curves of refrigerants by molecular simulation," Fluid Phase Equilibria **375**, 143–151 (2014).

[52] C. M. Colina and E. A. Müller, "Molecular simulation of Joule-Thomson inversion curves," Int. J. Thermophys. **20**, 229–235 (1999).

[53] C. Colina and E. A. Müller, "Joule-Thomson inversion curves by molecular simulation," Molecular Simulation **19**, 237–246 (1997).

[54] C. M. Colina, M. Lisal, F. R. Siperstein, and K. E. Gubbins, "Accurate CO_2 Joule-Thomson inversion curve by molecular simulations," Fluid Phase Equilibria **202**, 253–262 (2002).

[55] A. Chacin, J. Vazquez, and E. Müller, "Molecular simulation of the Joule–Thomson inversion curve of carbon dioxide," Fluid Phase Equilibria **165**, 147–155 (1999).

[56] M. Lagache, P. Ungerer, and A. Boutin, "Prediction of thermodynamic derivative properties of natural condensate gases at high pressure by Monte Carlo simulation," Fluid Phase Equilibria **220**, 211–223 (2004).

[57] E. A. Guggenheim, "The principle of corresponding states," The Journal of Chemical Physics **13**, 253–261 (1945).

[58] K. S. Pitzer, "Corresponding states for perfect liquids," The Journal of Chemical Physics **7**, 583–590 (1939).

[59] P. Orea, A. Romero-Martinez, E. Basurto, C. A. Vargas, and G. Odriozola, "Corresponding states law for a generalized Lennard-Jones potential," The Journal of Chemical Physics **143**, 024504 (2015).

[60] J. Vrabec, M. Kettler, and H. Hasse, "Chemical potential of quadrupolar two-centre Lennard-Jones fluids by gradual insertion," Chemical Physics Letters **356**, 431–436 (2002).

[61] E. Mason and T. Spurling, *The Virial Equation of State* (Pergamon Press, Oxford, 1969).

[62] T. L. Hill, *An Introduction to Statistical Thermodynamics* (Dover Publications, New York, 1986).

[63] D. A. McQuarrie, *Statistical Mechanics* (Harper & Row, New York, 1976).

[64] L. Shampine, "Vectorized adaptive quadrature in MATLAB," Journal of Computational and Applied Mathematics **211**, 131–140 (2008).

[65] R. Fingerhut, G. Guevara-Carrion, I. Nitzke, D. Saric, J. Marx, K. Langenbach, S. Prokopev, D. Celný, M. Bernreuther, S. Stephan, M. Kohns, H. Hasse, and J. Vrabec, "ms2: A molecular simulation tool for thermodynamic properties, release 4.0," Computer Physics Communications **262**, 107860 (2021).

[66]G. Rutkai, A. Köster, G. Guevara-Carrion, T. Janzen, M. Schappals, C. W. Glass, M. Bernreuther, A. Wafai, S. Stephan, M. Kohns, S. Reiser, S. Deublein, M. Horsch, H. Hasse, and J. Vrabec, "ms2: A molecular simulation tool for thermodynamic properties, release 3.0," Computer Physics Communications **221**, 343–351 (2017).

[67]R. Lustig, "Statistical analogues for fundamental equation of state derivatives," Molecular Physics **110**, 3041–3052 (2012).

[68]R. Lustig, "Direct molecular NVT simulation of the isobaric heat capacity, speed of sound and Joule-Thomson coefficient," Mol. Simul. **37**, 457–465 (2011).

[69]K. R. S. Shaul, A. J. Schultz, and D. A. Kofke, "The effect of truncation and shift on virial coefficients of Lennard-Jones potentials," Collection of Czechoslovak Chemical Communications **75**, 447–462 (2010).

[70]D. Fertig and S. Stephan, "Influence of dispersive long-range interactions on transport and excess propertiesof simple mixtures," Molecular Physics , e2162993 (2023).

[71]S. Stephan and H. Hasse, "Influence of dispersive long-range interactions on properties of vapour-liquid equilibria and interfaces of binary Lennard-Jones mixtures," Molecular Physics **118**, e1699185 (2020).

[72]M. P. Allen and D. J. Tildesley, *Computer Simulation of Liquids* (Oxford University Press, Oxford, 1989).

[73]I. Nezbeda, "Simulations of vapor-liquid equilibria: Routine versus thoroughness," Journal of Chemical & Engineering Data **61**, 3964–3969 (2016).

[74]S. Pohl, R. Fingerhut, M. Thol, J. Vrabec, and R. Span, "Equation of state for the Mie $(\lambda_r,6)$ fluid with a repulsive exponent from 11 to 13," The Journal of Chemical Physics **158**, 084506 (2023).